www.czasopisma.pan.pl PAN POLSKA AKADEMIA NAUK www.journals.pan.pl

Arch. Metall. Mater. **63** (2018), 3, 1481-1484

DOI: 10.24425/123834

S.-M. YONG*#, D.H. CHOI*, K. LEE*, S.-Y. KO*, D.-I. CHEONG*

INFLUENCE OF THE CALCINATION TEMPERATURE ON THE OPTICAL AND MECHANICAL PROPERTIES OF Y_2O_3-MgO NANOCOMPOSITES

Y_2O_3-MgO nanocomposites are one of the most promising materials for hypersonic infrared windows and domes due to their excellent optical transmittance and mechanical properties. In this study, influence of the calcination temperature of Y_2O_3-MgO nanopowders on the microstructure, IR transmittance, and hardness of Y_2O_3-MgO nanocomposites was investigated. It was found that the calcination temperature is related to the presence of residual intergranular pores and grain size after spark plasma sintering. The nanopowders calcined at 1000°C exhibits the highest infrared transmittance (82.3% at 5.3 μm) and hardness (9.99 GPa). These findings indicated that initial particle size and distribution of the nanopowders are important factors determining the optical and mechanical performances of Y_2O_3-MgO nanocomposites.

Keywords: Infrared transparent ceramics, Y_2O_3-MgO nanocomposites, sol-gel combustion synthesis, calcination, spark plasma sintering

1. Introduction

Y_2O_3-MgO nanocomposites have recently received much attention as one of the most promising candidate materials for hypersonic infrared (IR) windows and domes [1-4]. In these nanocomposites, the presence of one phase naturally impedes the grain growth of the adjacent phase. This is known as the pinning effect, which is most effective when the ceramic phases have comparable volume fractions and are dispersed uniformly in the composites. The reduced grain size can increase the optical transparency, especially when the grain size is smaller than the wavelength of the incident light (less than approximately $\lambda/20$). In addition, a smaller grain size increases the mechanical strength and thermal shock resistance [5,6]. Thus, Y_2O_3-MgO nanocomposites exhibit optical and mechanical properties superior to those of other IR transparent materials, such as Al_2O_3, $MgAl_2O_4$, AlON, and Y_2O_3 [7].

It is important that both the synthesis and sintering conditions of composite nanopowders are well controlled to fabricate the nanocomposites with fine grains and homogeneous microstructures. Several methods for synthesizing high-quality composite nanopowders have been developed, such as the sol-gel [1-4], flame spray pyrolysis, coprecipitation [5,7-9], and glycine-nitrate process [10]. Among these, the sol-gel method is superior to other methods due to its low processing temperature, low cost, precise control of the composition, and homogeneous phase distribution. Wang et al. [1] reported the use of the sol-gel combustion method to synthesize the Y_2O_3-MgO composite nanopowders. They obtained a white gel by mixing the Y and Mg precursors in deionized water and followed by a drying step. Additional combustion and calcination processes were then conducted for the decomposition of the metal precursors and for decarbonization, resulting in an Y_2O_3-MgO composite nanopowder with a small particle size and a homogeneous microstructure. Recently, chelating agents, such as citric acid [4,11], glucose [3], and sucrose [12] have been used to form stable metal complexes.

It is difficult to obtain excellent optical and mechanical properties with Y_2O_3-MgO nanocomposites when using the conventional pressureless sintering process. Kear et al. [5] reported that a sample sintered in air at 1600°C for 5 h showed a density level of less than 95%. After re-heating to 1700°C in air for 5 h, the density increased to nearly 100%, but the grain size increased to approximately 10 μm. In general, therefore, the densification of transparent nanocomposites is conducted using hot pressing (HP), hot isostatic pressing (HIP), and spark plasma sintering (SPS) techniques, all of which apply a load during the process. The SPS technique has a significant advantages over the HP and HIP because it can complete the densification within a short sintering time owing to the application of a high electric field (typical heating rate >50°C/min) [13-15]. There are few studies of the SPS of Y_2O_3-MgO nanocomposite. Xu et al. [11] and Jiang et al. [16] studied the influence of SPS and the post-sinter annealing conditions on the optical transmittance of

* THE 4TH RESEARCH AND DEVELOPMENT INSITITUTE-4, AGENCY OF DEFENSE DEVELOPMENT (ADD), YUSEONG P.O. BOX 35, DAEJEON 34186, REPUBLIC OF KOREA

Corresponding author: y990906@hanmail.net

these composites. Huang et al. [9] investigated the effect of SPS temperature on the mechanical properties.

In the present study, the influence of the calcination temperature of Y_2O_3-MgO nanopowders on the microstructure, IR transmittance, and hardness of the Y_2O_3-MgO nanocomposites was investigated. The sol-gel combustion method was adopted to synthesize the Y_2O_3-MgO nanopowders. The synthesized Y_2O_3-MgO nanopowders were consolidated using the SPS technique.

2. Experimental

Y_2O_3-MgO nanopowder was synthesized using the sol-gel combustion method. Details of the nanopowder synthesis approach are described in the literature [1]. Yttrium nitrate ($Y(NO_3)_3 \cdot 6H_2O$) and magnesium acetate ($(CH_3COO)_2Mg \cdot 4H_2O$), corresponding to Y_2O_3 and MgO at a volume ratio of 50:50, were dissolved in deionized water under mild magnetic stirring at room temperature. The above solution was dried in a preheated electric oven at 200°C for 36 h. The dried gel was then heated in a box furnace to 600 ~ 1200°C (heating rate of 5°C/min) with a holding time of 2 h. The heat-treated powder was ball-milled with ZrO_2 balls in anhydrous alcohol for 24 h. The slurry was dried at 80°C and sieved through a 200-mesh screen.

Densification of the as-prepared nanopowder was carried out using a SPS system under a vacuum (~6 Pa). The nanopowder was loaded into a graphite die with graphite foils at both ends, and heated from room temperature to a 1200°C at a heating rate of 50°C/min under a uniaxial pressure of 50 MPa. It was held for 5 min before turning off the power. The temperature was controlled by an optical pyrometer focused on the outer surface of the sintering die. Post-sinter annealing was conducted at 1100°C for 20 h in air. The annealed samples were then mirror-polished on both surfaces for further characterization and investigation.

The thermal characteristics of the dried gel were analyzed using a TGA instrument (SDT Q600, TA Instruments, USA). Transmission electron microscopy (TEM, JEM-3010, JEOL, Japan) was utilized to observe the morphology of the synthesized Y_2O_3-MgO nanopowder. The crystalline phase of the synthesized Y_2O_3-MgO nanopowder was characterized by X-ray diffractometer (XRD, D/MAX-2500, Rigaku, Japan) with Cu Ka radiation. The microstructure of the sintered samples was examined by scanning electron microscopy (FE-SEM, Quanta 650, FEI, Netherlands). For the SEM observation, mirror-polished samples were thermally etched at 1100°C for 1 h in air. The grain size was determined by counting the number of grains in the SEM micrograph. Assuming the grains to be spherical, the average grain size was determined to be 1.225 times the apparent grain size [17]. Fourier transform infrared spectroscopy (FTIR, Nicolet iS50, Thermo Scientific, USA) was used to measure the transmittance of the sintered sample in the range of 400 ~ 4000 cm^{-1}. The hardness was measured using a Vickers hardness tester (VLPAK2000, Mitutoyo, Japan) with a load of 2 kg on the surface.

In this paper, C-X denotes the synthesized Y_2O_3-MgO nanopowder calcined at X°C, while the sample sintered using C-X is denoted by S-C-X.

3. Results and discussion

Typical TG/DTA curves of the dried gel at a heating rate of 5°C/min are shown in Fig. 1. In the temperature range of 250 to 420°C, a drastic weight loss of approximately 55% and two exothermic peaks (at 310 and 397°C) are clearly observed. These are ascribed to the pyrolysis of the yttrium and magnesium precursors [1]. At temperatures higher than 420°C, no significant weight loss was noted, indicating that the pyrolysis process was complete.

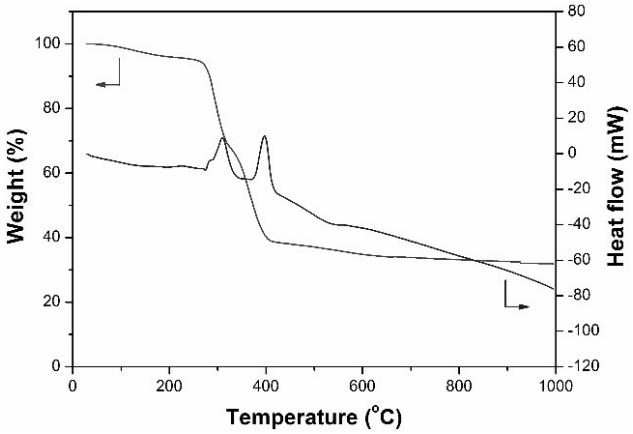

Fig. 1. Typical TG/DTA curves of the dried gel (a heating rate of 5°C/min)

The XRD patterns of the synthesized Y_2O_3-MgO nanopowders are shown in Fig. 2. The synthesized nanopowders are composed of cubic Y_2O_3 (JCPDS No. 72-0927) and MgO (JCPDS No. 74-1225) phases, regardless of the calcination temperature. Other materials as impurities were not found. It was noted that the values of the full width at half maximum (FWHM)

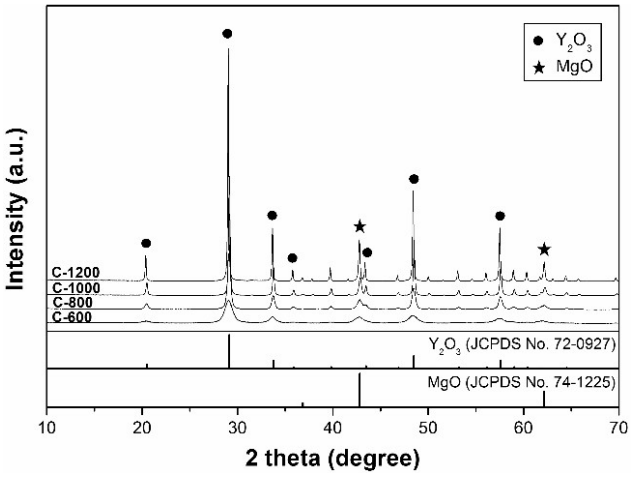

Fig. 2. XRD patterns of the synthesized Y_2O_3-MgO nanopowders

of the Y_2O_3 and MgO peaks gradually become narrow with an increase in the calcination temperature, indicating an increase in the crystallinity.

The TEM micrographs of the synthesized Y_2O_3-MgO nanopowders are shown in Fig. 3. C-600 consists of nanoparticles less than 10 nm in size. When the calcination temperature increases to 800, 1000, and 1200°C, the average particle size also increases to about 21.64, 33.70, and 68.82 nm, respectively.

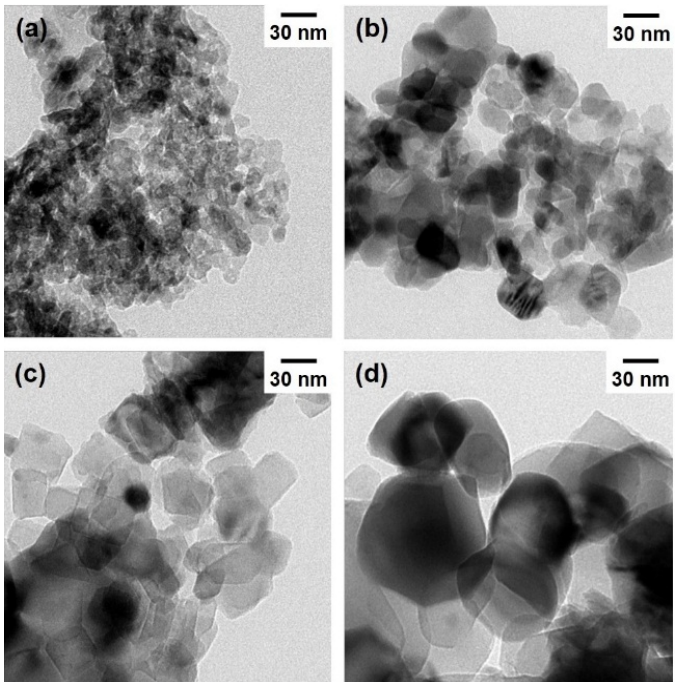

Fig. 3. TEM micrographs of the synthesized Y_2O_3-MgO nanopowders: (a) C-600, (b) C-800, (C) C-1000, and (d) C-1200

The SEM micrographs of the fabricated Y_2O_3-MgO nanocomposites are shown in Fig. 4. The bright grains are the Y_2O_3 phase and the dark grains are the MgO phase. The average grain sizes of S-C-600, 800, 1000, and 1200 are 121.3, 131.3, 127.13, and 171.4 nm, respectively. For S-C-600 and 800, many large pores were found to remain at the grain boundary junctions. These may be internal pores within the highly agglomerated nanoparticles of C-600 and 800. Owing to the high sinterability of the small primary nanoparticles, the internal pores within the agglomerates would be readily closed and difficult to eliminate in the subsequent densification process [18], resulting in the formation of the residual intergranular pores. For S-C-1000 and 1200, on the other hand, only a few fine pores were occasionally observed, meaning that C-1000 and 1200 are relatively favorable for obtaining full densification. This can be attributed to the reduced number of internal pores within the agglomerates caused by the increase in the primary particle size.

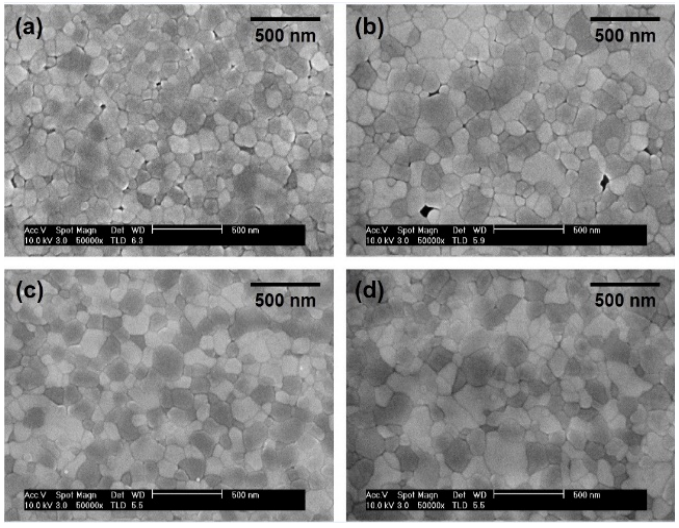

Fig. 4. SEM micrographs of the fabricated Y_2O_3-MgO nanocomposites: (a) S-C-600, (b) S-C-800, (C) S-C-1000, and (d) S-C-1200

Fig. 5 shows the IR transmittance spectra of the fabricated Y_2O_3-MgO nanocomposites. S-C-1000 exhibits higher transmittance in the mid-IR range as compared to the other samples. S-C-600, 800, and 1000 exhibit their highest transmittances of 80.9, 79.7, and 82.3% at 5.3 μm, respectively. With a decrease in the wavelength, however, the transmittances of S-C-600 and 800 decrease more sharply than that of S-C-1000. This may be attributed to the scattering at the intergranular pores caused by the large difference in the refractive index between the nanocomposite and the pores [7]. In the case of S-C-1200, the transmittance in the mid-IR range is lower than those of the other samples, possibly due to an increase in the grain boundary scattering stemming from the relatively large grain size [5]. All samples exhibit the absorption peaks at the same wavelengths. The absorption peak near 7 μm is attributed to asymmetrical and symmetrical stretching vibrations of the carboxylate group, which is contributed to not only residual carbonate after calcination and annealing but also carbon contamination from the graphite die. A weak absorption peak at 4.28 μm is associated with CO_2 in the environment [10].

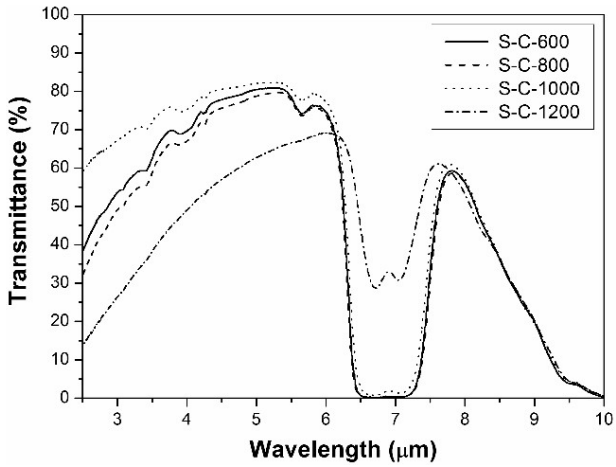

Fig. 5. IR transmittance spectra of the fabricated Y_2O_3-MgO nanocomposites

To investigate the mechanical properties of the fabricated Y_2O_3-MgO nanocomposite, the Vickers hardness was measured. Fig. 6 displays the hardness as a function of the calcination temperature. The hardness levels of S-C-600, 800, 1000, and

1200 are 9.66, 9.20, 9.99, and 9.14, respectively. Compared with S-C-1000, the other samples exhibit the relatively lower hardness levels, as in the relationship between the transmittance and the calcination temperature. In general, the hardness is mainly influenced by the grain size and the pores. For a large grain size, a small number of grain boundaries cannot act as obstacles to dislocation movement, resulting in low hardness levels (Hall-Petch relationship [9]). Moreover, high porosity leads to a decrease in the hardness. These are why the hardness levels of S-C-600, 800, and 1200 degrade.

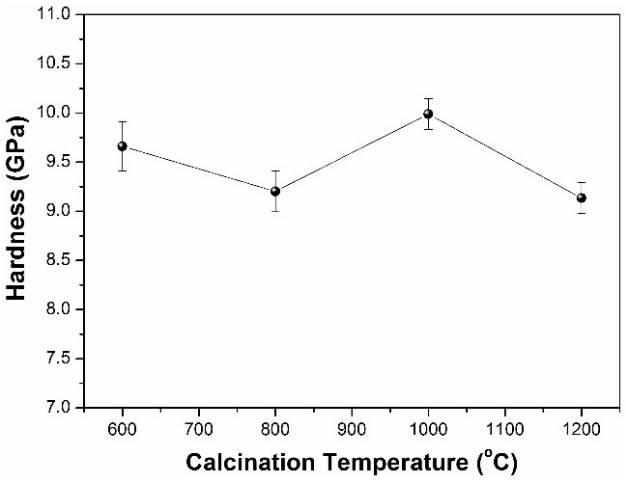

Fig. 6. Hardness as a function of the calcination temperature of the fabricated Y_2O_3-MgO nanocomposites

4. Conclusions

In this study, the influence of the calcination temperature of Y_2O_3-MgO nanopowders on the microstructure, IR transmittance, and hardness of the Y_2O_3-MgO nanocomposites was investigated. It was demonstrated that the calcination temperature affected the residual intergranular pores and the grain size after the densification using SPS. The highest IR transmittance (82.3% at 5.3 μm) and hardness (9.99 GPa) were achieved from the nanopowder calcined at 1000°C, which was attributed to the small grain size and the relatively few residual intergranular pores. This result indicated that the initial particle size and distribution of the nanopowders are important factors determining the optical and mechanical performances of the Y_2O_3-MgO nanocomposites. It is also expected that the optical transmittance and mechanical properties can be improved by modifying and optimizing the powder synthesis and sintering conditions.

Acknowledgments

This work was supported by DAPA and ADD.

REFERENCES

[1] J. Wang, D. Chen, E.H. Jordan, M. Gell, J. Am. Ceram. Soc. **93** (11), 3535-3538 (2010).

[2] S. Xu, J. Li, C. Li, Y. Pan, J. Guo, J. Am. Ceram. Soc. **98** (3), 1019-1026 (2015).

[3] S. Xu, J. Li, C. Li, Y. Pan, J. Guo, J. Am. Ceram. Soc. **98** (9), 2796-2802 (2015).

[4] J. Xie, X. Mao, X. Li, B. Jiang, L. Zhang, Ceram. Int. **43**, 40-44 (2017).

[5] B.H. Kear, R. Sadangi, V. Shukla, T. Stefanik. R. Gentilman, Proc. of SPIE **5786**, 227-233 (2005).

[6] J. Wang, L. Zhang, D. Chen, E.H. Jordan, M. Gell, J. Am. Ceram. Soc. **95** (3), 1033-1037 (2012).

[7] D.C. Harris, L.R. Cambrea, L.F. Johnson, R.T. Seaver, M. Baronowski, R. Gentilman, C.S. Nordahl, T. Gattuso, S. Silberstein, P. Rogan, T. Hartnett, B. Zelinski, W. Sunne, E. Fest, W.H. Poisl, C.B. Willingham, G. Turri, C. Warren, M. Bass, D.E. Zelmon, S.M. Goodrich, J. Am. Ceram. Soc. **96** (12). 3828-3835 (2013).

[8] T. Stefanik, R. Gentilman, P. Hogan, Proc. of SPIE **6545**, 65450A (2007).

[9] L. Huang, W. Yao, J. Liu, A.K. Mukherjee, J.M. Schoenung, Scr. Mater. **75**, 18-21 (2014).

[10] H.J. Ma, W.K. Jung, C. Baek, D.K. Kim, J. Eur. Ceram. Soc. **37**, 4902-4911 (2017).

[11] S. Xu, J. Li, H. Kou, Y. Shi, Y. Pan, J. Guo, Ceram. Int. **41**, 3312-3317 (2015).

[12] A. Iyer, J.K.M. Garofano, J. Reutenaur, S.L. Suib, M. Aindow, M. Gell, E.H. Jordan, J. Am. Ceram. Soc. **96** (2), 346-350 (2013).

[13] K. Morita, B.-N. Kim, K. Hiraga, H. Yoshida, Scr. Mater. **58**, 1114-1117 (2008).

[14] K.T. Kim, T. Min, D.W. Kim, J. Korean Powder Metall. Inst. **23**, 263-269 (2016).

[15] J.-K. Han, D.-W. Shin, B. Madavali, S.-J. Hong, J. Korean Powder Metall. Inst. **24**, 115-121 (2017).

[16] D.T. Jiang, A.K. Mukherjee, J. Am. Ceram. Soc. **93** (3), 769-773 (2010).

[17] R. Apetz, M.P.B. van Bruggen, J. Am. Ceram. Soc. **86** (3), 480-486 (2003).

[18] B. Liu, J. Li, M. Ivanov, W. Liu, J. Liu, T. Xie, S. Zhou, Y. Pai, J. Guo, Opt. Mater. **36**, 1591-1597 (2014).